ACS OMEGA

Open Access

This article is licensed under CC-BY-NC-ND 4.0

http://pubs.acs.org/journal/acsodf

Article

Ultralow Power Electronic Analog of a Biological Fitzhugh–Nagumo Neuron

Ragib Ahsan, Zezhi Wu, Seyedeh Atiyeh Abbasi Jalal, and Rehan Kapadia*

Cite This: *ACS Omega* 2024, 9, 18062–18071

Read Online

ACCESS | Metrics & More | Article Recommendations | Supporting Information

ABSTRACT: Here, we introduce an electronic circuit that mimics the functionality of a biological spiking neuron following the Fitzhugh–Nagumo (FN) model. The circuit consists of a tunnel diode that exhibits negative differential resistance (NDR) and an active inductive element implemented by a single MOSFET. The FN neuron converts a DC voltage excitation into voltage spikes analogous to biological action potentials. We predict an energy cost of 2 aJ/cycle through detailed simulation and modeling for these FN neurons. Such an FN neuron is CMOS compatible and enables ultralow power oscillatory and spiking neural network hardware. We demonstrate that FN neurons can be used for oscillator-based computing in a coupled oscillator network to form an oscillator Ising machine (OIM) that can solve computationally hard NP-complete max-cut problems while showing robustness toward process variations.

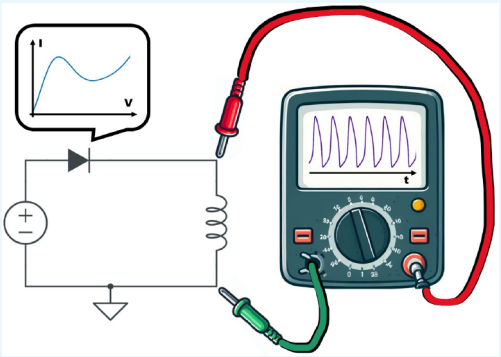

INTRODUCTION

Biological brains can perform computational tasks at an ~100,000× efficiency compared to the digital computers.[1−6] A typical biological neuron has a surface area of ~10 μm^2, spends ~10 pJ energy to generate each spike, and operates at a frequency of ~100 Hz, which translates to a power cost of ~1 nW for biological systems.[3,4,6] The first set of efforts in emulating biological neurons dates back to 1960s following the FN model using voltage controlled NDR devices[7,8] paired with inductors to produce relaxation oscillations similar to neuronal spiking behavior.[9−11] The inductor element is the main scaling bottleneck of this circuit implementation of spiking neuron, as coil-based passive inductors are difficult to fabricate at nanoscale with the required inductance values. The emergence of current-controlled NDR devices featuring metal–insulator phase transition materials has enabled generation of relaxation oscillations using capacitors, leading to considerable progress in artificial spiking neurons.[12−23] There have been other approaches to producing NDR, such as band to band tunneling, resonant tunneling, Gunn effect, real space electron transfer in III–V heterostructures, body biasing of MOSFET, exploiting graphene's unique dispersion relationship near its Dirac point, using trap-based recombination processes, redox behavior of molecular junctions, and multiple circuits.[7,8,24−42] Recently, we have shown that a graphene–silicon photodetector can show voltage-dependent NDR behavior under optical illumination while operating in the photovoltaic regime.[43] This photosensor coupled with an inductive circuit element generates optically driven voltage oscillations similar to those of ganglion cells in the retina, following the FN model of spiking neurons. Using a frequency multiplexed parallel computing approach, these oscillatory retinal neurons (ORNs) were then used to demonstrate ultralow-power in-sensor neuronal computing for machine vision. Purely electronic oscillatory neurons can extend the ability of FN neurons to different types of sensors and enable the construction of deep oscillator-based neural networks. In addition, electronic oscillatory neurons are instrumental to traditional oscillatory neural networks (ONNs), where a network of coupled oscillators can be used as associative memory[44−58] or an engine for convolution-like operations.[44,45,59−62] However, there are three important challenges to achieving ultralow power oscillator-based computing: (1) scalability, (2) energy consumption, and (3) variability of the oscillatory neurons. These neurons serve as the smallest unit of computation in oscillator networks similar to the different logic gates in digital computing systems. Therefore, a cohesive effort is necessary to improve the design of individual neuron circuits and the algorithms that would allow the employment of these neurons for the promised excellent performance of the brain-inspired computing architectures.

In this work, we have introduced an FN neuron implementation with a tunnel diode and an active inductor. The scaling bottleneck presented by passive inductors is removed in this implementation of the FN neuron by using the active inductor that can easily be fabricated at nanoscale by

Received: December 12, 2023
Revised: March 14, 2024
Accepted: March 26, 2024
Published: April 9, 2024

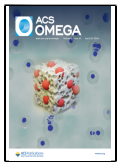

ACS Publications

© 2024 The Authors. Published by American Chemical Society

https://doi.org/10.1021/acsomega.3c09936
ACS Omega 2024, 9, 18062–18071

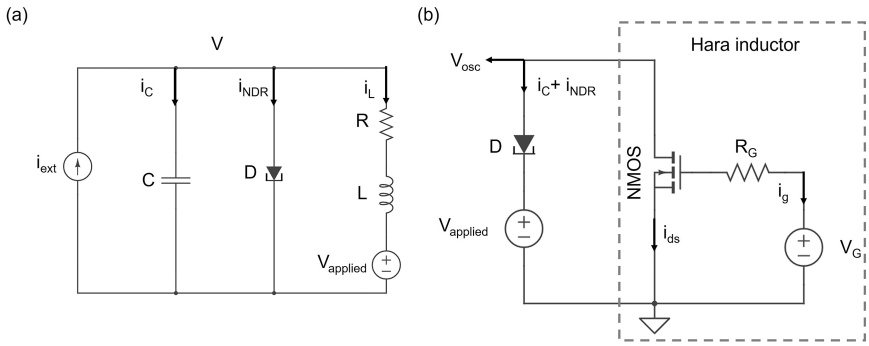

Figure 1. Implementation of an FN neuron. (a) Equivalent circuit of an FN neuron using a tunnel diode. (b) Circuit schematic of an FN neuron using Hara inductor.

traditional CMOS processes. The active inductor emulates the behavior of a passive coil-based inductor by taking advantage of an active element: a single MOSFET, and a resistor. Through circuit simulations, we demonstrated the oscillation behavior of the FN neuron implemented using this active inductor and predicted the scalability limits. The key feature of this neuron is that it is expected to generate voltage spikes with ∼2 aJ/cycle energy cost, whereas the Mott transition-based neurons consume an electrical energy of ∼50 pJ/cycle, and the state-of-the-art CMOS neuron consumes ∼4 fJ/cycle.[12,14,17−21,23] These FN neurons can generate firing patterns similar to biological neurons. We have then used FN neurons to form a coupled oscillator network onto which a computationally hard combinatorial problem such as max-cut problem can be mapped in an Ising machine-like fashion. This OIM can then minimize the Ising Hamiltonian associated with the max-cut problem and identify correct solutions while consuming a small electrical energy.

RESULTS AND DISCUSSION

The spiking behavior of biological neurons was first described by the Hodgkin−Huxley (HH) model. The HH model interprets the dynamics of ion flows across neuronal membrane and the resulting generation and propagation of action potentials through a set of coupled differential equations. The Fitzhugh−Nagumo (FN) model reduces the complexity of the HH model by using just two variables: the membrane potential and the recovery variable. Despite its simplicity, the FN model captures some of the essential features of the Hodgkin−Huxley model, such as the concept of a threshold for firing an action potential and the recovery of the membrane potential after firing. Moreover, the FN model can reproduce many of the behaviors observed in the Hodgkin−Huxley model such as the propagation of action potentials and the refractory period. Dynamics of Fitzhugh−Nagumo neurons can be described by the following coupled differential equations:[63]

$$\frac{dv}{dt} = f(v) - w + ri_{ext}$$

$$\tau\frac{dw}{dt} = v + a - bw$$

Here, v is reminiscent of the membrane potential of a neuron, which is excited by an external stimulus i_{ext} analogous to the ion pump current through a nonlinear medium $f(v)$. $f(v)$ can be simplified as a third-order polynomial. Such an excitation is then dissipated through a slower sink w. Figure S1a shows the nullclines and the trajectory of the system for $f(v) = v - \frac{v^3}{3}$ for parameter values of $(a, b, r, \tau, i_{ext}) = (0.7, 0.8, 0.5, 12.5, 0.4)$. Figure S1b shows the waveforms obtained for the Fitzhugh−Nagumo neurons for different values of i_{ext}, showing that action potentials or spikes are not generated for under-excitation or over-excitation conditions. Figure S2 shows the nullclines and trajectories of the system under different parameter values.

Here, we develop a circuit to emulate FN neurons, with the equivalent circuit shown in Figure 1a, with the third-order nonlinear element $f(v)$ approximated by a tunnel diode, a circuit element that exhibits negative differential resistance. The following coupled differential equations describe the dynamics of this circuit:

$$C\frac{dV}{dt} = -i_{NDR}(V) - i_L + i_{ext}$$

$$L\frac{di_L}{dt} = V + V_{applied} - Ri_L$$

These equations are equivalent to those of the Fitzhugh−Nagumo neurons and differ only by a scaling factor. In the absence of the resistor R and the offset DC voltage $V_{applied}$, this circuit would simplify to a more traditional Van der Pol oscillator.[64−66] While such a circuit accurately captures the description of a Fitzhugh−Nagumo neuron, the presence of an inductor in the circuit limits its implementation and scalability.

To overcome this challenge, we explore the effect of implementing this circuit with a Hara active inductor comprising a single FET and a resistor.[67−69] Figure 1b shows the circuit schematic for an FN neuron by using the Hara inductor and a tunnel diode. The parasitic capacitance of the tunnel diode (C) is implicit here. There are two sources of electrical power in this circuit: V_G and $V_{applied}$. However, impedance of the series R_G−C_{gs} branch is $R_G + \frac{1}{j\omega C_{gs}}$, which blocks any DC current flow, and therefore power consumption in the V_G source is zero. Therefore, all of the power in this neuron comes from the source, $V_{applied}$. This power can be calculated from

$$P_{osc} = -\frac{1}{T}\int_0^T V_{applied}(i_{NDR} + i_C)\,dt$$
$$= -\frac{1}{T}\int_0^T V_{applied} i_{NDR}\,dt,$$

where T is the period of one fundamental oscillation. Here, the capacitive current integrates to zero over a full cycle of oscillation. The energy in each cycle can be calculated from

https://doi.org/10.1021/acsomega.3c09936
ACS Omega 2024, 9, 18062−18071

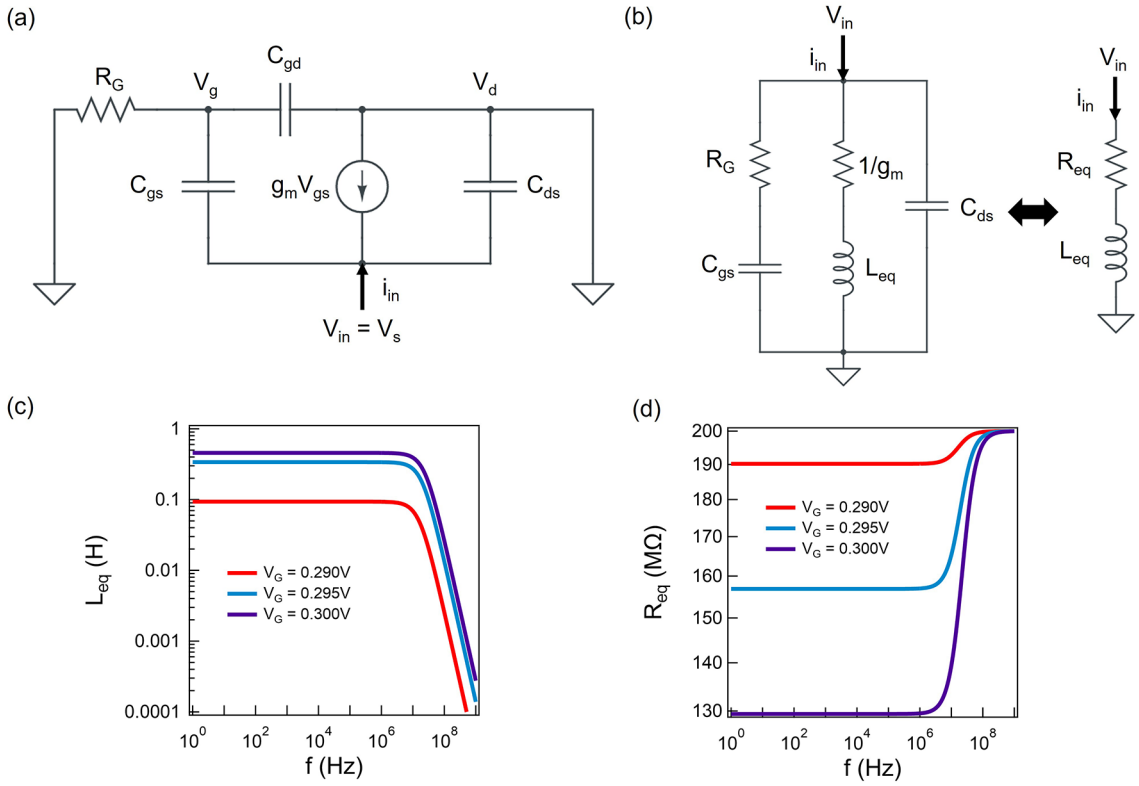

Figure 2. Small signal behavior of the Hara inductor. (a) Small signal model for Hara inductor and (b) equivalent circuit. (c) Equivalent inductance and (d) series resistance of Hara inductor using a 65 nm process MOSFET with W/L = 1 and R_G = 200 MΩ.

$E_{osc} = P_{osc}T$. As a rule of thumb, the power consumptions in both the tunnel diode and active inductor are $\sim I_{peak}V_{peak}$, where I_{peak} is the peak current of the tunnel diode before the start of the NDR regime, and V_{peak} is the voltage at which I_{peak} is observed. Since I_{peak} decreases linearly with tunnel diode device area, any reduction in power and energy consumption requires us to scale down the diode to the smallest possible size.

The nonlinear element in the FN neuron does not necessarily have to be a tunnel diode, as there are many different CMOS compatible circuit topologies that allow NDR with a small footprint. However, a tunnel diode is also a CMOS compatible device that allows aggressive scaling to the nanometer scale. Figure S3a shows the experimentally measured $J-V$ and $C-V$ curves of a silicon tunnel diode.[70] We have considered a linear scaling behavior between diode current and physical diode area, which is a reasonable assumption for tunnel diodes as discussed in Section S2.1. This silicon tunnel diode is composed of a vertically stacked p^{++} ($\sim 10^{20}$ cm^{-3})/n^{++} ($\sim 10^{20}$ cm^{-3}) silicon homojunction, completely compatible with CMOS fabrication processes. As discussed in Section S2.2, a large peak current density of 1.75 $\mu A/\mu m^2$ indicates that a tunnel diode can be scaled down to 100 nm × 100 nm size while keeping a ~30 dB signal-to-noise ratio at 1 GHz bandwidth. In addition to tunnel diodes that achieve NDR behavior through band-to-band tunneling, resonant tunneling diodes (RTDs) utilizing the resonant tunneling phenomenon in multiple quantum well-like structures can also be used in this implementation of FN neurons. Due to the near unity transmission probability for carriers, Si/SiGe-based RTDs can achieve a much higher NDR peak current density (2.18 $mA/\mu m^2$)[42] compared to tunnel diodes while maintaining similar capacitance per area. As a result, an RTD-based oscillator can potentially reach a much higher oscillation frequency.[36,38,39,41] Recently, RTDs have therefore been explored for designing spiking neurons for applications in neuromorphic computing.[35,37,40] However, fabrication of RTDs is more complicated, since RTDs are heterojunction devices. It is also more difficult to achieve NDR behavior in RTDs at room temperature due to its inherent physics. On the other hand, the simplified fabrication process, increased variation tolerance, and comparatively smaller susceptibility to thermal noise of silicon tunnel diodes make them better candidates for practical implementation of FN neurons.

Figure 2a,b shows a small signal equivalent circuit for the Hara inductor. The small signal model gives us an equivalent inductance of $L_{eq} = \frac{R_G C_{gs}}{g_m}$, where R_G is the series resistance to the gate, C_{gs} is the gate to source capacitance of the FET, and g_m is the transconductance of the FET.[67,69] The DC voltage source in series to the gate determines the bias point and consequently g_m of the FET. However, it is important to note that the spiking neuron operation can lead to voltage swings of ~100 mV, and the small signal model would not be applicable in that case. Nevertheless, it is a good starting point to design the neuron circuit regardless of the nonidealities introduced by the large signal voltage swings. Figure 2c shows L_{eq} as a function of operating frequency for a 65 nm CMOS process MOSFET with W/L = 1 at different bias voltages and R_G = 200 MΩ. Figure 2d shows the equivalent resistance seen at the input terminal. These results show that L_{eq} can be tuned by the bias voltage. However, an active inductor has a positive equivalent inductance only within a certain frequency range, which puts certain design constraints on the FN neuron.

https://doi.org/10.1021/acsomega.3c09936
ACS Omega 2024, 9, 18062−18071

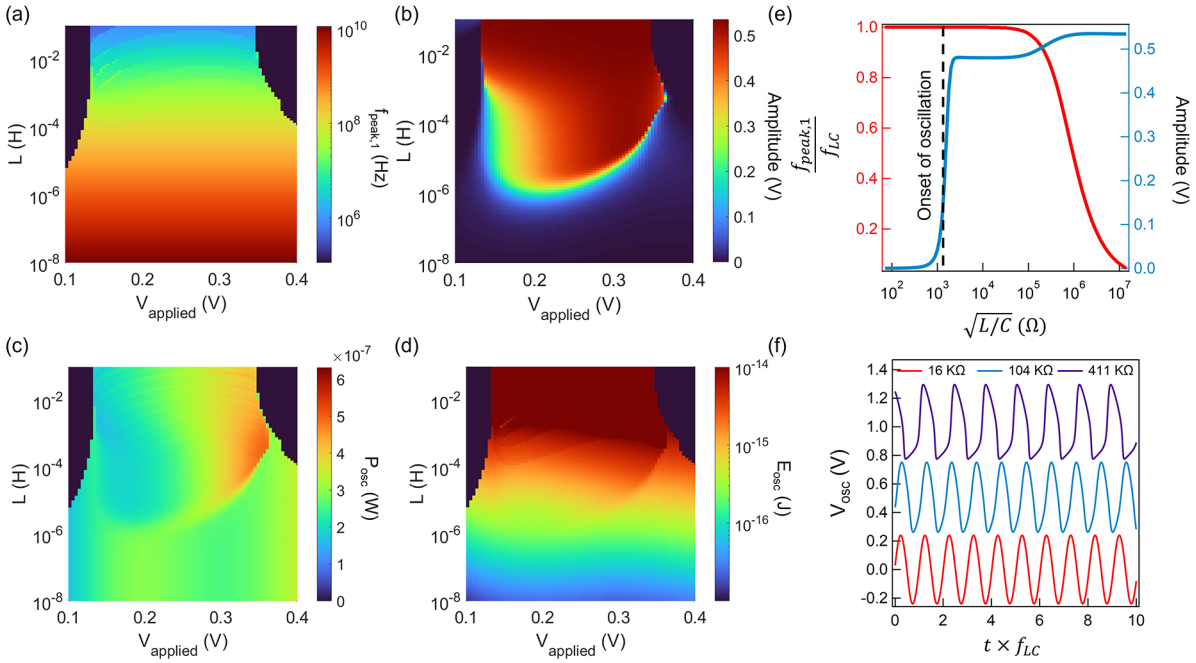

Figure 3. Simulated oscillation behavior of a silicon tunnel-diode-based FN neuron. Colormaps of (a) fundamental oscillation frequency, (b) amplitude, (c) power, and (d) energy consumption in the FN neuron using passive inductors. (e) Normalized fundamental oscillation frequency and amplitude of the FN neuron. (f) Typical oscillation waveforms at different $\sqrt{L/C}$ values.

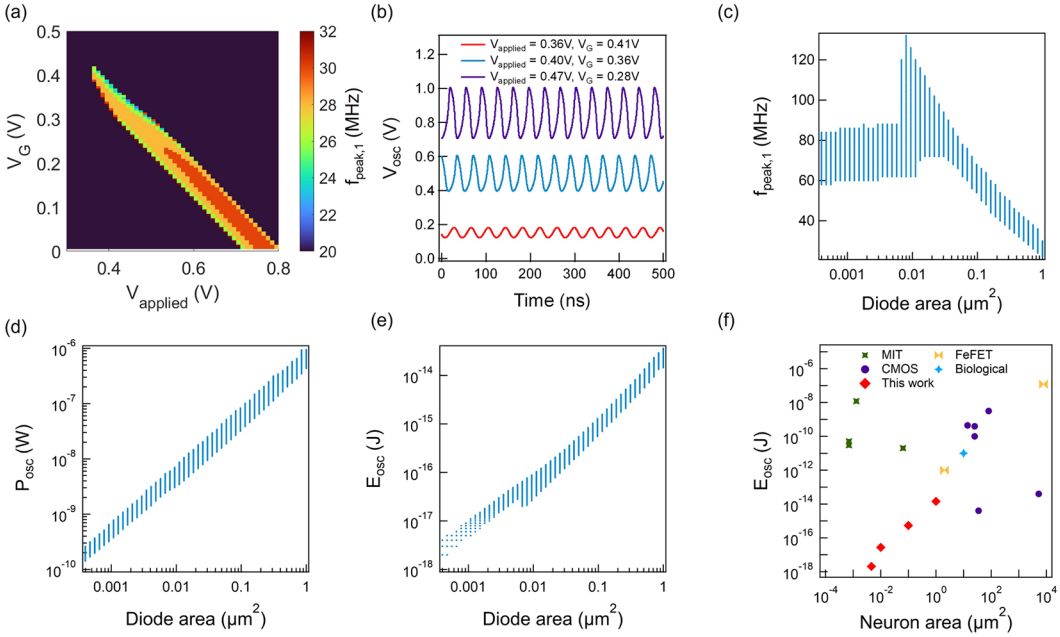

Figure 4. Simulated oscillation behavior of FN neuron implemented with the Hara inductor. (a) Colormap of fundamental oscillation frequency. (b) Example oscillation waveforms at different conditions. (c) Fundamental oscillation frequency, (d) power, and (e) energy consumption as a function of diode area. (f) Energy cost comparison with other artificial spiking neuron technologies.

Using the established behavior of the individual elements, we combine them to form the FN neuron, as shown in Figure 1a. We have performed circuit simulations for a FN neuron using the $I-V$ curve and device capacitance obtained from the experimental data of a silicon tunnel diode and an ideal inductor with no series resistance (ideal Van der Pol oscillator case). The experimentally obtained $I-V$ curve was first mathematically fit and then interpolated to generate a lookup table. Using a lookup table allows us to speed up simulations by avoiding evaluation of the nonlinear function as we solve the system of ordinary differential equations at each time step. Figure 3a–d shows the colormaps for oscillation amplitude, frequency, power consumption, and energy consumption, respectively, for a diode of 1 μm^2 device area. We observe from these colormaps that oscillation is only possible within certain applied voltage ranges, and the oscillation amplitude is significant after a threshold inductance. These values are functions of the tunnel diode $I-V$ curve as oscillations can only be sustained at the voltages for

https://doi.org/10.1021/acsomega.3c09936
ACS Omega 2024, 9, 18062−18071

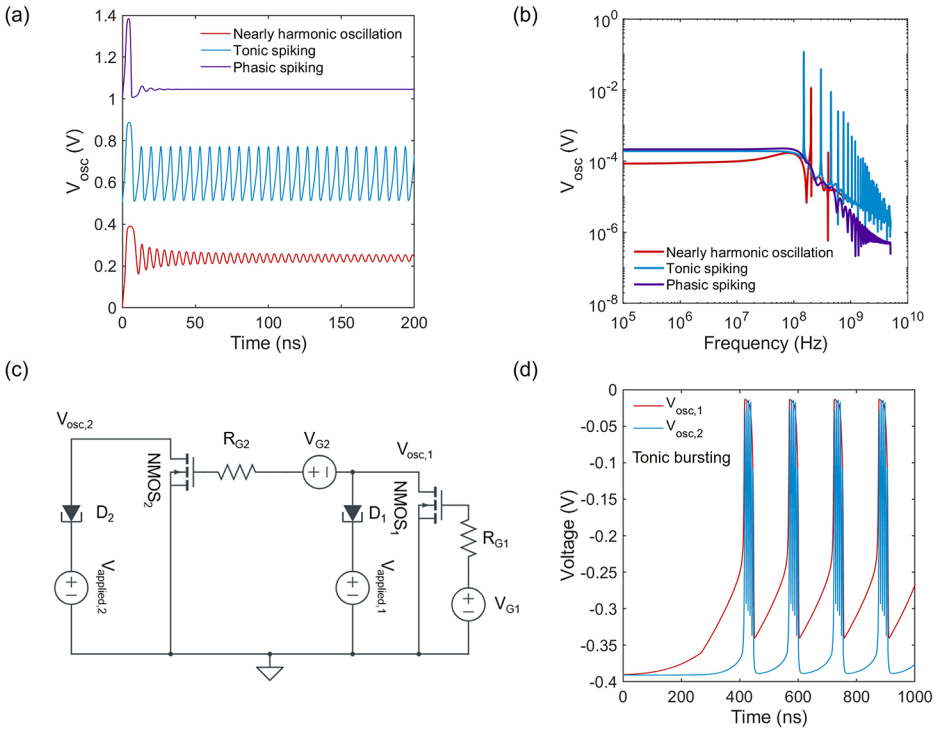

Figure 5. Biological neuron-like firing patterns. (a) Firing patterns of a single FN neuron showing tonic and phasic spiking and (b) corresponding FFT spectra. (c) Circuit schematic of two cascaded FN neurons. (d) Tonic bursting patterns generated by the cascaded circuit.

which NDR behavior exists. We have then introduced a normalized quantity $\sqrt{\frac{L}{C}}$ analogous to the characteristic impedance of a transmission line. When the device area (A) decreases, both the current and capacitance of the diode decrease linearly. This quantity captures the effect of scaling both the device area and inductance. Figure 3e shows the fundamental oscillation frequency ($f_{\text{peak},1}$) normalized to the resonant frequency of the LC circuit ($f_{\text{LC}} = \frac{1}{2\pi\sqrt{LC}}$) and oscillation amplitude for $V_{\text{applied}} = 0.4$ V. We can observe a sharp increase in oscillation amplitude at $\sqrt{\frac{L}{C}} \approx 1$ KΩ clearly marking the onset of oscillation. It is noteworthy that such an oscillator approximates an LC oscillator for $\sqrt{\frac{L}{C}} < 100$ KΩ, where $f_{\text{peak},1} \approx f_{\text{LC}}$. Figure 3f shows some example oscillation waveforms for the FN neurons at different values of $\sqrt{\frac{L}{C}}$, where we can observe the emergence of sharp spikes as we keep increasing $\sqrt{\frac{L}{C}}$. As we scale the tunnel diode down to smaller sizes, both I and C will scale linearly, and we would need to increase the inductance L linearly to maintain the same oscillation threshold and frequency. For a tunnel diode with an area of 1 μm^2, $C = 25$ fF, we would need an inductance of ∼100 nH to start the oscillations.

In order to understand the scaling limits of this FN neuron, we have then simulated the Hara inductor-based neurons using the 65 nm CMOS process-based MOSFET.[71] It is important to note that while a 65 nm MOSFET has been used here for these simulations, quantitatively similar results can be obtained by using any other FET such as 5 nm FINFETs. Since the inductive load depends on R_G, C_{gs}, and g_m ($L_{eq} = \frac{R_G C_{gs}}{g_m}$), FETs of different sizes and processes can achieve the same inductance by adjusting their transconductance (g_m) by applying an appropriate V_G so that $\frac{C_{gs}}{g_m}$ ratio remains constant. In addition, the capacitive load seen by the oscillator is a parallel combination of the parasitic capacitance of the diode and the drain-to-source capacitance (C_{ds}) of the FET. Since C_{ds} is typically much smaller (∼100×) compared to diode capacitance, the operational frequency of the oscillator will not be affected significantly by using different FETs as long as $C_{\text{diode}} \gg C_{ds}$. Figure 4a shows the oscillation frequency colormap for a FN neuron comprising a 1 μm^2 tunnel diode and $R_G = 200$ MΩ. As shown in Figure 4a, there is a particular range of V_G and V_{applied} values at which spiking neural behavior can be sustained. A decrease in V_G decreases the inductance and increases the series resistance. As a result, we see a larger oscillation frequency at a smaller V_G. However, the increasing series resistance requires us to increase V_{applied} to sustain oscillation. Figure 4b shows some oscillation waveforms for different V_G and V_{applied}. We then performed the same simulation for tunnel diodes of different device areas between 400 nm^2 and 1 μm^2. Figure 4c shows $f_{\text{peak},1}$ as a function of diode area, showing an ∼80 MHz oscillation frequency for the smallest devices. Figure 4d,e shows the P_{osc} and E_{osc} for the FN neuron for a minimum oscillation amplitude of 50 mV. P_{osc} and E_{osc} are calculated using the following equations,

$$P_{\text{osc}} = \frac{1}{T}\int_0^T V_{\text{applied}} i_{\text{NDR}}\, \mathrm{d}t$$

$$E_{\text{osc}} = \int_0^T V_{\text{applied}} i_{\text{NDR}}\, \mathrm{d}t$$

Here, T is the fundamental oscillation period. The decrease in P_{osc} and E_{osc} is linear to the neuron area until the MOSFET area becomes the limiting factor. For a 0.0046 μm^2 neuron area (20

https://doi.org/10.1021/acsomega.3c09936
ACS Omega 2024, 9, 18062−18071

nm × 20 nm diode, 65 nm × 65 nm MOSFET), we estimate a P_{osc} of 1.4 nW and a E_{osc} of 2 aJ, which is the lowest among reported energy per oscillation cycle for different electronic neurons.[6,12−15,17,18,22,34,72−78] It is important to note that the spread in the data comes from all possible oscillation conditions at different V_G and $V_{applied}$. The current flow and operation voltage for this FN neuron implementation depend on the tunnel diode $I-V$ characteristics. As discussed in more detail in Section S5, we do not expect any significant influence of the FET sizing or process on the oscillation frequency or amplitude and therefore also on power and energy consumption. Figure 4f shows the comparison between the energy consumption per cycle for different types of neurons found in the literature. There are mainly three other approaches to making an artificial neuron: (1) metal−insulator transition (MIT) memristors and a capacitor, (2) circuit-based techniques implemented with CMOS technology, and (3) ferroelectric FETs (FeFETs) with a regular FET. While the MIT neurons can be scaled down to ∼1000 nm^2, the minimum energy cost is ∼50 pJ for oscillation, which is significantly larger compared to that of biological neurons.[6,12−15,17,18,22,72] CMOS-based neurons have a large distribution of power and energy costs depending on the circuit techniques used for implementing the spiking neural behavior.[34,73−78] Current state-of-the-art spiking neuron[75] has a 35 μm^2 area with a 4 fJ energy consumption, whereas a typical biological neuron of ∼10 μm^2 area has an energy consumption of ∼10 pJ. FeFET neurons also demonstrate promise in achieving oscillation with an energy cost of ∼1 pJ. In contrast to all these artificial neurons, our proposed FN neuron consumes an electrical energy of 2 aJ, which can further the state-of-the-art of this field.

An FN neuron is a two-dimensional dynamical system capable of showing several biological neuron-like firing patterns, such as phasic and tonic spiking. Excitability of an FN neuron is dependent on the design parameters. Figure 5a shows three different operations of an FN neuron with a diode area of 0.02 μm^2, R_G = 110 MΩ, $V_{applied}$ = 0.39 V, and three different values of V_G. At smaller V_G (0.1 V), transconductance of the FET is smaller, and the Hara inductor presents a large inductive impedance. As a result, the nonlinear term in the FN neuron model becomes smaller, and the FN neuron shows nearly harmonic oscillations. As V_G becomes larger (0.2 V), inductive impedance becomes smaller, and the oscillations become more nonlinear with sharper spiking nature. This is similar to tonic spiking in biological neurons. When V_G becomes even larger (0.35 V), the neuron shows a transient spike, followed by overdamped oscillations similar to phasic spiking patterns. Figure 5b shows the corresponding FFT spectra of the oscillation time series shown in Figure 5a. As expected, the nearly harmonic oscillations show much smaller high harmonic peaks compared to the fundamental frequency, while the tonic spiking pattern shows significantly larger high harmonic contents. The phasic spiking pattern does not show any significant frequency peak as the oscillation dies away with time. It is important to note that FN neuron model inherently lacks the capability to generate bursting patterns due to its limited dimensionality. However, it is possible to cascade two FN neurons, as shown in Figure 5c to increase the dimensionality and generate tonic bursting patterns (Figure 5d). Essentially, when the oscillations generated by one neuron are much slower than the other (R_{G1} = 100R_{G2} = 11 GΩ), it is possible to modulate the V_{G2} input of the second neuron using the output of the first neuron ($V_{osc,1}$). As a result, the second neuron only fires when the first neuron provides the necessary voltage. Therefore, it is possible to generate different firing patterns by designing electronic circuits with multiple FN neurons.

FN neurons can be used to create traditional spiking neural networks (SNNs) for performing tasks typical of artificial neural networks (ANNs). These traditional SNN architectures encode information in the timing (temporal encoding) or frequency (rate encoding) of spiking patterns and make use of all-or-nothing spiking dynamical behavior of neurons to process information.[79−81] These architectures typically mimic the behavior of ANNs while utilizing the low energy consumption behavior of spiking neurons. Performance of these networks has been further limited by their incompatibility with back-propagation methods of learning. The dimensionality of these networks is reduced due to their all-or-nothing spiking nature. On the other hand, oscillator-based computing approaches utilizing synchronization behavior of oscillator networks through interaction can potentially make use of a much richer computational space to perform more versatile tasks. A liquid state machine comprising a network of oscillators is theoretically capable of performing all tasks doable by a Turing machine without resorting to any learning mechanism.[82−87] OIMs have been used to solve computationally hard combinatorial problems by exploiting the oscillation dynamics of a coupled oscillator network. In our previous work, we have shown that it is possible to perform massively parallel computing by multiplexing operations in the frequency domain. SNNs are therefore a subset of the massive computational space offered by computing systems by using oscillator dynamics.

While an oscillatory neuron is the building block for neuromorphic oscillatory computing, the actual computation emerges from the macroscopic behavior of a network of coupled oscillators. Harnessing these emergent computational behaviors is contingent on the construction of the coupling network. There have been prior works on associative memory property of coupled oscillators where the oscillator phases settle to certain values resulting from the minimization of the "energy" of the system.[44,45,47,50,55,61,62] OIM is a special case of such a phase-based computation scheme, where a computationally hard combinatorial optimization problem can be mapped to the coupling impedances of the oscillator network. Under certain circumstances, the oscillators would then settle to a combination of binary phases (0 or π) that result in a minimization of the system energy that corresponds to the Ising Hamiltonian of the problem.[55−58] Typically, the oscillator phases can take continuous values between 0 and π. However, if the oscillators are externally injected with a signal with twice their fundamental oscillation frequency, it is possible to force them to have binary phase differences of 0 or π because of subharmonic injection locking (SHIL).[55−57] Detailed mathematical analysis on mapping NP-hard and NP-complete combinatorial problems to OIMs has been carried out elsewhere.[44,55−58,62] This work focuses on how FN neurons can be utilized for oscillator-based computing, and we have chosen to demonstrate how an FN neuron-based OIM can be used to solve an NP-complete problem such as the "max-cut" problem. If we have a graph with N-nodes and the nodes have M-edges between them with different weights, then the max-cut problem aims to find a binary partition between the N-nodes that results in the maximum number of cuts to the edge weights. For the sake of simplicity, let us consider a graph with 2-nodes with a single edge with unity weight. Then, partitioning the two nodes into different groups

https://doi.org/10.1021/acsomega.3c09936
ACS Omega 2024, 9, 18062−18071

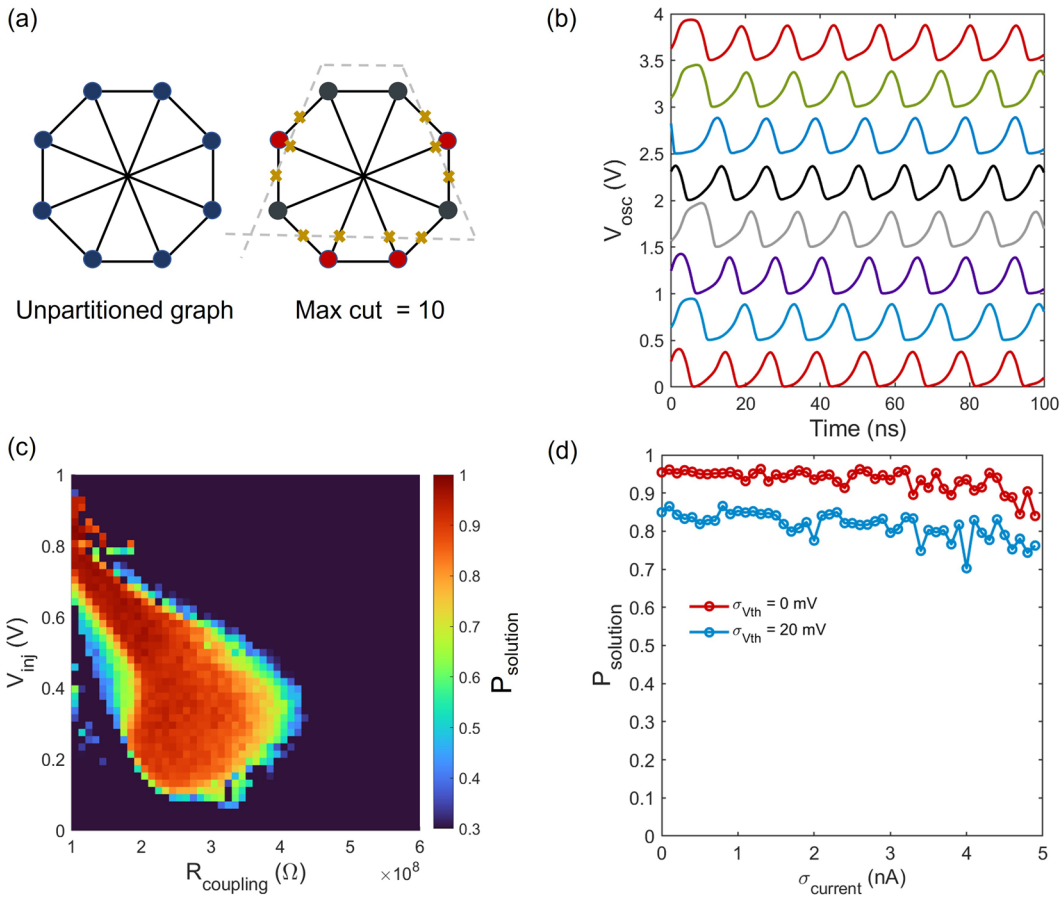

Figure 6. Implementation of an Ising machine with FN neurons. (a) A 8-node graph for max-cut problem and its solution. (b) Evolution of oscillation waveforms toward correct solution from random initial conditions. (c) Colormap of solution probability as a function of $R_{coupling}$ and V_{inj} without considering any variation. (f) Robustness of $P_{solution}$ to variations in tunnel diode current.

results in the max-cut of 1 (Figure S5a). Figure S5b shows how this problem can be mapped on two FN neurons coupled with a resistor, $R_{coupling}$. When $R_{coupling}$ is too small, the oscillators are always in phase, and there is no partition between the oscillators. On the other hand, when $R_{coupling}$ is large, the oscillators are almost uncoupled, and therefore they do not maintain a specific phase difference between them. However, for intermediate values of $R_{coupling}$, they would always couple with a phase difference of π, resulting in a partition. We have performed simulations for X different random initial conditions for the FN neurons for a given $R_{coupling}$ and then calculated the probability of finding correct solution as $P_{solution} = \frac{\#\text{ instances leading to correct solution}}{X}$. Figure S5c shows $P_{solution}$ as a function of $R_{coupling}$ for V_{inj} = 0.5 V and R_{SHIL} = 50 MΩ (X = 1000). Figure S5d shows evolution of the oscillation waveform toward the correct solution, i.e., coupling antiphase. It is noteworthy that the symbol of oscillator includes the FN neuron as well as an externally applied SHIL signal, as shown in Figure S6a.

Figure 6a shows the graph for an 8-node max-cut problem and the solution that yields maximum cuts of 10. Figure S6b shows the circuit schematic implementing this max-cut problem. Here, we consider $R_{ij} = R_{coupling}$ for all values of (i,j). Figure 6b shows the evolution of oscillator phases toward the partition that gives us maximum cuts. This result was achieved for $R_{coupling}$ = 150 MΩ, R_{SHIL} = 50 MΩ, and V_{inj} = 0.5 V for f_{SHIL} = 150 MHz. It is important to note that $P_{solution}$ is heavily dependent on the parameters of the coupling network. The correct partition between oscillators depends critically on two factors: (1) the ability to achieve phase bipartition and (2) the ability to achieve the correct order of phase bipartition. While phase bipartition ability comes explicitly from the SHIL signal and therefore depends on the strength of V_{inj}, the correct order of phase bipartition comes from the coupling between different oscillators and hence on $R_{coupling}$. Figure 6c shows the colormap of $P_{solution}$ as a function of $R_{coupling}$ and V_{inj} for R_{SHIL} = 50 MΩ (X = 768). As shown in Figure 6c, high values of $P_{solution}$ can be achieved only when the combination of $R_{coupling}$ and V_{inj} is within a certain range. However, one of the key issues with implementing OIMs is the variation between the oscillators. Since the phase bipartition is very sensitive to the oscillation dynamics, variations in oscillators can lead to significant degradation of $P_{solution}$. For nanoscale devices, these variations are more pronounced due to random dopant fluctuation, lithography-based size variations, etc. Random dopant variation is most pronounced since ion implantation in CMOS processes is inherently a stochastic process, and such variation leads to significant spread in threshold voltages across different MOSFETs. In addition, the tunnel diodes also feature heavily doped p^{++} ($>10^{19}$ cm^{-3}) and n^{++} regions ($>10^{19}$ cm^{-3}). Therefore, we can also expect some variations in the tunnel diode current levels. However, when there is current flow in a diode, its capacitance is dominated by the charge transport capacitance or diffusion capacitance. This capacitance is directly

https://doi.org/10.1021/acsomega.3c09936
ACS Omega 2024, 9, 18062−18071

proportional to current, and therefore, such current variations also lead to linear variations in device capacitance. As discussed in Section S6, when there is a variation in both device current and capacitance, the differential equation governing the oscillation dynamics remains immune to these fluctuations when the fluctuations are small. We have then introduced a Gaussian variation in both device current and capacitance of the tunnel diodes for the 8-node max-cut circuit and simulated the OIM oscillation dynamics. Figure 6d shows $P_{solution}$ as a function of standard deviation ($\sigma_{current}$) in tunnel diode peak current, showing the insensitivity of $P_{solution}$ as $\sigma_{current}$ increases. When we consider variations in V_{th} ($\sigma_{V_{th}}$ = 20 mV), as experimentally observed in a previous study on 65 nm MOSFETs,[88] there is a slight degradation in $P_{solution}$ as shown in Figure 5d. These results clearly show the promise of FN neurons in oscillator-based computing. While CMOS compatibility and scalability would allow realization of large scale coupled oscillator networks, electrical energy consumption of such networks can also be minimized because of the superior energy efficiency of FN neurons.

CONCLUSION

In conclusion, we have demonstrated an active inductor-based implementation for an FN neuron and predicted the scaling behavior of this neuron through simulations. Our simulations show that it is possible to generate the oscillation behavior in these neurons at an extremely low energy cost of 2 aJ per cycle. These FN neurons can generate firing patterns similar to biological neurons, such as tonic and phasic spiking. Firing patterns unachievable by a single FN neuron, such as bursting patterns, can also be generated by designing appropriate circuits with these neurons. FN neurons can be used in a coupled oscillator network to form an Ising machine and solve NP-complete combinatorial problems such as the max-cut problem while being robust to process variations. This work shows a roadmap to designing and implementing FN neurons through voltage controlled NDR devices, replacing the real inductor with the MOSFET-based inductor, generation of oscillations with ultralow electrical energy, and possible application in large scale variation insensitive oscillator-based computing systems.

ASSOCIATED CONTENT

Data Availability Statement

The data that support the plots within this paper and other findings of this study are publicly available at https://doi.org/10.6084/m9.figshare.25405207.

Supporting Information

The Supporting Information is available free of charge at https://pubs.acs.org/doi/10.1021/acsomega.3c09936.

Additional details about theoretical modeling of FN neuron and Ising machine; nullclines and trajectory of a FN neuron (Figure S1); FN neuron nullclines and trajectories for different values of I_{ext} (Figure S2); experimentally measured $J-V$ and $C-V$ curves of a silicon tunnel diode, peak current density of silicon homojunction, and GaSb/InAs heterojunction tunnel diodes of different diode areas (Figure S3); oscillation, frequency, amplitude, power consumption, and energy consumption for different NMOS areas (Figure S4); simple 2-node max-cut problem and mapping 2-node max-cut problem to FN neurons (Figure S5); symbol for oscillator circuit and the actual circuit (Figure S6) (PDF)

AUTHOR INFORMATION

Corresponding Author

Rehan Kapadia − *Department of Electrical and Computer Engineering, University of Southern California, Los Angeles 90089-0001, United States;* orcid.org/0000-0002-7611-0551; Email: rkapadia@usc.edu

Authors

Ragib Ahsan − *Department of Electrical and Computer Engineering, University of Southern California, Los Angeles 90089-0001, United States;* orcid.org/0000-0002-3833-7851

Zezhi Wu − *Department of Electrical and Computer Engineering, University of Southern California, Los Angeles 90089-0001, United States*

Seyedeh Atiyeh Abbasi Jalal − *Department of Electrical and Computer Engineering, University of Southern California, Los Angeles 90089-0001, United States*

Complete contact information is available at: https://pubs.acs.org/10.1021/acsomega.3c09936

Author Contributions

R.A. and R.K. conceived the project. R.A., Z.W., and S.A.A.J performed the simulations. All authors contributed to analyzing the data. R.A. and R.K. wrote the paper while all the authors provided feedback.

Funding

1. Department of Energy Grant No. DE-SC0022248. 2. National Science Foundation Award No. 2004791. 3. Office of Naval Research Grant No. N00014−21−1−2634. 4. Air Force Office of Scientific Research Grant No. FA9550−21−1−0305.

Notes

The authors declare no competing financial interest.

ACKNOWLEDGMENTS

R.A. acknowledges USC Provost Graduate Fellowship. Z.W. acknowledges Viterbi Graduate School Fellowship.

REFERENCES

(1) Benjamin, B. V.; Gao, P.; McQuinn, E.; Choudhary, S.; Chandrasekaran, A. R.; Bussat, J.-M.; Alvarez-Icaza, R.; Arthur, J. V.; Merolla, P. A.; Boahen, K. Neurogrid: A Mixed-Analog-Digital Multichip System for Large-Scale Neural Simulations. *Proc. IEEE* **2014**, *102* (5), 699−716.

(2) Liu, S. C.; Delbrück, T.. *Introduction to Neuromorphic and Bio-Inspired Mixed-Signal VLSI*; California Institute of Technology: Pasadena, CA, 2007.

(3) Attwell, D.; Laughlin, S. B. An Energy Budget for Signaling in the Grey Matter of the Brain. *J. Cereb. Blood Flow Metab.* **2001**, *21* (10), 1133−1145.

(4) Lennie, P. The Cost of Cortical Computation. *Curr. Biol.* **2003**, *13* (6), 493−497.

(5) Oliveira, A.. *The digital mind: how science is redefining humanity*; MIT Press, 2017.

(6) Poon, C.-S.; Zhou, K. Neuromorphic silicon neurons and large-scale neural networks: challenges and opportunities. *Front. Neurosci.* **2011**, *5*, 108.

(7) Esaki, L. New Phenomenon in Narrow Germanium p-n Junctions. *Phys. Rev.* **1958**, *109* (2), 603−604.

(8) Gunn, J. B. Microwave oscillations of current in III−V semiconductors. *Solid State Commun.* **1963**, *1* (4), 88−91.

(9) Nagumo, J.; Arimoto, S.; Yoshizawa, S. An active pulse transmission line simulating nerve axon. *Proc. IRE* **1962**, *50* (10), 2061−2070.

(10) Nishizawa, J.-I.; Hayasaka, A. Two-line neuristor with active element in series and in parallel. *Int. J. Electron.* **1969**, *26* (5), 437−469.
(11) Crane, H.. *The neuristor*; IEEE, 1961; Vol. *4*, pp 3031.
(12) Duan, Q.; Jing, Z.; Zou, X.; Wang, Y.; Yang, K.; Zhang, T.; Wu, S.; Huang, R.; Yang, Y. Spiking neurons with spatiotemporal dynamics and gain modulation for monolithically integrated memristive neural networks. *Nat. Commun.* **2020**, *11* (1), 1−13.
(13) Wang, Z.; Joshi, S.; Savel'ev, S.; Song, W.; Midya, R.; Li, Y.; Rao, M.; Yan, P.; Asapu, S.; Zhuo, Y.; et al.et al. Fully memristive neural networks for pattern classification with unsupervised learning. *Nat Electron.* **2018**, *1* (2), 137−145.
(14) Jerry, M.; Parihar, A.; Grisafe, B.; Raychowdhury, A.; Datta, S.. *Ultra-low power probabilistic IMT neurons for stochastic sampling machines*; IEEE, 2017; pp T186T187.
(15) Tuma, T.; Pantazi, A.; Le Gallo, M.; Sebastian, A.; Eleftheriou, E. Stochastic phase-change neurons. *Nat. Nanotechnol.* **2016**, *11* (8), 693−699.
(16) Lim, H.; Ahn, H.-W.; Kornijcuk, V.; Kim, G.; Seok, J. Y.; Kim, I.; Hwang, C. S.; Jeong, D. S. Relaxation oscillator-realized artificial electronic neurons, their responses, and noise. *Nanoscale* **2016**, *8* (18), 9629−9640.
(17) Lee, D.; Kwak, M.; Moon, K.; Choi, W.; Park, J.; Yoo, J.; Song, J.; Lim, S.; Sung, C.; Banerjee, W.; et al.et al. Various threshold switching devices for integrate and fire neuron applications. *Adv. Electron. Mater.* **2019**, *5* (9), 1800866.
(18) Pickett, M. D.; Medeiros-Ribeiro, G.; Williams, R. S. A scalable neuristor built with Mott memristors. *Nat. Mater.* **2013**, *12* (2), 114−117.
(19) Stoliar, P.; Tranchant, J.; Corraze, B.; Janod, E.; Besland, M. P.; Tesler, F.; Rozenberg, M.; Cario, L. A leaky-integrate-and-fire neuron analog realized with a Mott insulator. *Adv. Funct. Mater.* **2017**, *27* (11), 1604740.
(20) Mehonic, A.; Kenyon, A. J. Emulating the electrical activity of the neuron using a silicon oxide RRAM cell. *Front. Neurosci.* **2016**, *10*, 57.
(21) Gupta, I.; Serb, A.; Khiat, A.; Zeitler, R.; Vassanelli, S.; Prodromakis, T. Real-time encoding and compression of neuronal spikes by metal-oxide memristors. *Nat. Commun.* **2016**, *7* (1), 1−9.
(22) Huang, H.-M.; Yang, R.; Tan, Z.-H.; He, H.-K.; Zhou, W.; Xiong, J.; Guo, X. Quasi-Hodgkin−Huxley Neurons with Leaky Integrate-and-Fire Functions Physically Realized with Memristive Devices. *Adv. Mater.* **2019**, *31* (3), 1803849.
(23) Ignatov, M.; Ziegler, M.; Hansen, M.; Petraru, A.; Kohlstedt, H. A memristive spiking neuron with firing rate coding. *Front. Neurosci.* **2015**, *9*, 376.
(24) Hess, K.; Morkoç, H.; Shichijo, H.; Streetman, B. G. Negative differential resistance through real-space electron transfer. *Appl. Phys. Lett.* **1979**, *35* (6), 469−471.
(25) Ho, C.-L.; Wu, M.-C.; Ho, W.-J.; Liaw, J.-W. Light-induced negative differential resistance in planar InP/InGaAs/InP double-heterojunction p-i-n photodiode. *Appl. Phys. Lett* **1999**, *74* (26), 4008−4010.
(26) Vega-González, V.; Gutiérrez-Domínguez, E.; Guarin, F. A negative differential resistance effect implemented with a single MOSFET from 375 k down to 80 k. In *2013 Proceedings of the European Solid-State Device Research Conference (ESSDERC)*; IEEE, 2013; pp 330333. DOI: .
(27) Sharma, P.; Bernard, L. S.; Bazigos, A.; Magrez, A.; Ionescu, A. M. Room-Temperature Negative Differential Resistance in Graphene Field Effect Transistors: Experiments and Theory. *ACS Nano* **2015**, *9* (1), 620−625.
(28) Wu, Y.; Farmer, D. B.; Zhu, W.; Han, S.-J.; Dimitrakopoulos, C. D.; Bol, A. A.; Avouris, P.; Lin, Y.-M. Three-Terminal Graphene Negative Differential Resistance Devices. *ACS Nano* **2012**, *6* (3), 2610−2616.
(29) Chen, H.; Nie, H.; Guo, L. Interface trap-induced negative differential resistance in nMOSFET with floating source. *Phys. Lett. A* **2020**, *384* (17), 126342.
(30) Hourdakis, E.; Kaidatzis, A.; Niarchos, D.; Nassiopoulou, A. G. Voltage-controlled negative differential resistance in metal-sputtered alumina-Si structures. *J. Phys. D: Appl. Phys.* **2019**, *52* (8), 085101.
(31) Liu, W.; Guo, H.; Li, W.; Wan, X.; Bodepudi, S. C.; Shehzad, K.; Xu, Y. Light-induced negative differential resistance in gate-controlled graphene-silicon photodiode. *Appl. Phys. Lett.* **2018**, *112* (20), 201109.
(32) Wang, X.; Wang, Y.; Feng, M.; Wang, K.; Bai, P.; Tian, Y. Light-induced negative differential resistance effect in a resistive switching memory device. *Curr. Appl. Phys.* **2020**, *20* (3), 371−378.
(33) Chen, J.; Reed, M. A.; Rawlett, A. M.; Tour, J. M. Large On-Off Ratios and Negative Differential Resistance in a Molecular Electronic Device. *Science* **1999**, *286* (5444), 1550−1552.
(34) Zhao, F.; Jia, C.; Guo, W.; Xie, S.; Chen, Y.; Tee, C. A. T. H.; Huo, D.; Chang, Y.; Jiang, H. Silicon neuron transistor based on CMOS negative differential resistance (NDR). *IEICE Electron. Express* **2020**, *17* (24), 20200316−20200316.
(35) Hejda, M.; Alanis, J. A.; Ortega-Piwonka, I.; Lourenço, J.; Figueiredo, J.; Javaloyes, J.; Romeira, B.; Hurtado, A. Resonant tunneling diode nano-optoelectronic excitable nodes for neuromorphic spike-based information processing. *Phys. Rev. Appl.* **2022**, *17* (2), 024072.
(36) Cimbri, D.; Wang, J.; Al-Khalidi, A.; Wasige, E. Resonant tunneling diodes high-speed terahertz wireless communications-A review. *IEEE Trans. Terahertz Sci. Technol.* **2022**, *12* (3), 226−244.
(37) Ortega-Piwonka, I.; Piro, O.; Figueiredo, J.; Romeira, B.; Javaloyes, J. Bursting and excitability in neuromorphic resonant tunneling diodes. *Phys. Rev. Appl.* **2021**, *15* (3), 034017.
(38) Feiginov, M. Frequency limitations of resonant-tunnelling diodes in sub-THz and THz oscillators and detectors. *J. Infrared, Millimeter, Terahertz Waves* **2019**, *40* (4), 365−394.
(39) Izumi, R.; Suzuki, S.; Asada, M.. 1.98 THz resonant-tunneling-diode oscillator with reduced conduction loss by thick antenna electrode. In *2017 42nd International Conference on Infrared, Millimeter, and Terahertz Waves (IRMMW-THz)*; IEEE, 2017; pp 12.
(40) Romeira, B.; Javaloyes, J.; Ironside, C. N.; Figueiredo, J. M.; Balle, S.; Piro, O. Excitability and optical pulse generation in semiconductor lasers driven by resonant tunneling diode photo-detectors. *Opt. Express* **2013**, *21* (18), 20931−20940.
(41) Suzuki, S.; Teranishi, A.; Hinata, K.; Asada, M.; Sugiyama, H.; Yokoyama, H. Fundamental oscillation of up to 831 GHz in GaInAs/AlAs resonant tunneling diode. *Appl. Phys. Express* **2009**, *2* (5), 054501.
(42) Chung, S.-Y.; Yu, R.; Jin, N.; Park, S.-Y.; Berger, P. R.; Thompson, P. E. Si/SiGe resonant interband tunnel diode with f/sub r0/20.2 GHz and peak current density 218 kA/cm/sup 2/for K-band mixed-signal applications. *IEEE Electron Device Lett.* **2006**, *27* (5), 364−367.
(43) Ahsan, R.; Chae, H. U.; Jalal, S. A. A.; Tao, J.; Das, S.; Liu, H.; Wu, J.-B.; Cronin, S.; Wang, H.; Sideris, C.; Kapadia, R.. *Ultra-low power in-sensor neuronal computing with oscillatory retinal neurons for frequency-multiplexed, parallel machine vision*; Research Square, 2023.
(44) Csaba, G.; Raychowdhury, A.; Datta, S.; Porod, W.. Computing with coupled oscillators: Theory, devices, and applications. In *2018 IEEE International Symposium on Circuits and Systems (ISCAS)*; IEEE, 2018; pp 15.
(45) Raychowdhury, A.; Parihar, A.; Smith, G. H.; Narayanan, V.; Csaba, G.; Jerry, M.; Porod, W.; Datta, S. Computing with networks of oscillatory dynamical systems. *Proc. IEEE* **2019**, *107* (1), 73−89.
(46) Pourahmad, V.; Manipatruni, S.; Nikonov, D.; Young, I.; Afshari, E. Nonboolean pattern recognition using chains of coupled CMOS oscillators as discriminant circuits. *IEEE J. Explor. Solid-State Comput. Devices Circuits* **2017**, *3*, 1−9.
(47) Nikonov, D. E.; Csaba, G.; Porod, W.; Shibata, T.; Voils, D.; Hammerstrom, D.; Young, I. A.; Bourianoff, G. I. Coupled-oscillator associative memory array operation for pattern recognition. *IEEE J. Explor. Solid-State Comput. Devices Circuits* **2015**, *1*, 85−93.
(48) Shibata, T.; Zhang, R.; Levitan, S. P.; Nikonov, D. E.; Bourianoff, G. I. CMOS supporting circuitries for nano-oscillator-based associative memories. In *2012 13th International Workshop on Cellular Nanoscale Networks and their Applications*; IEEE, 2012; pp. 15.

https://doi.org/10.1021/acsomega.3c09936
ACS Omega 2024, 9, 18062−18071

(49) Delacour, C.; Carapezzi, S.; Abernot, M.; Todri-Sanial, A.. *Energy-Performance Assessment of Oscillatory Neural Networks based on VO2 Devices for Future Edge AI Computing*; IEEE, 2022.
(50) Núñez, J.; Avedillo, M. J.; Jiménez, M.; Quintana, J. M.; Todri-Sanial, A.; Corti, E.; Karg, S.; Linares-Barranco, B. Oscillatory Neural Networks Using VO2 Based Phase Encoded Logic. *Front. Neurosci.* **2021**, *15*, 655823.
(51) Corti, E.; Cornejo Jimenez, J. A.; Niang, K. M.; Robertson, J.; Moselund, K. E.; Gotsmann, B.; Ionescu, A. M.; Karg, S. Coupled VO2 oscillators circuit as analog first layer filter in convolutional neural networks. *Front. Neurosci.* **2021**, *15*, 628254.
(52) Jackson, T.; Pagliarini, S.; Pileggi, L. An oscillatory neural network with programmable resistive synapses in 28 nm CMOS. In *2018 IEEE International Conference on Rebooting Computing (ICRC)*; IEEE, 2018; pp 17.
(53) Jackson, T. C.; Sharma, A. A.; Bain, J. A.; Weldon, J. A.; Pileggi, L. Oscillatory neural networks based on TMO nano-oscillators and multi-level RRAM cells. *IEEE J. Emerging Sel. Top. Circuits Sys.* **2015**, *5* (2), 230−241.
(54) Vaidya, J.; Surya Kanthi, R.; Shukla, N. Creating electronic oscillator-based Ising machines without external injection locking. *Sci. Rep.* **2022**, *12* (1), 981.
(55) Dutta, S.; Khanna, A.; Assoa, A.; Paik, H.; Schlom, D. G.; Toroczkai, Z.; Raychowdhury, A.; Datta, S. An Ising Hamiltonian solver based on coupled stochastic phase-transition nano-oscillators. *Nat. Electron.* **2021**, *4* (7), 502−512.
(56) Wang, T.; Roychowdhury, J. OIM: Oscillator-based Ising machines for solving combinatorial optimization problems. In *Unconventional Computation and Natural Computation: 18th International Conference, UCNC 2019, Tokyo, Japan, June 3−7, 2019, Proceedings*; Springer, 2019; pp 232256.
(57) Chou, J.; Bramhavar, S.; Ghosh, S.; Herzog, W. Analog coupled oscillator based weighted Ising machine. *Sci. Rep.* **2019**, *9* (1), 14786.
(58) Wang, T.; Wu, L.; Roychowdhury, J. New computational results and hardware prototypes for oscillator-based ising machines. In *Proceedings of the 56th Annual Design Automation Conference 2019*; arXiv, 2019; pp 12.
(59) Nikonov, D. E.; Kurahashi, P.; Ayers, J. S.; Li, H.; Kamgaing, T.; Dogiamis, G. C.; Lee, H.-J.; Fan, Y.; Young, I. Convolution inference via synchronization of a coupled CMOS oscillator array. *IEEE J. Explor. Solid-State Comput. Devices Circuits* **2020**, *6* (2), 170−176.
(60) Nikonov, D. E.; Young, I. A.; Bourianoff, G. I.. Convolutional networks for image processing by coupled oscillator arrays; arXiv. 2014.
(61) Koo, M.; Pufall, M.; Shim, Y.; Kos, A. B.; Csaba, G.; Porod, W.; Rippard, W.; Roy, K. Distance computation based on coupled spin-torque oscillators: Application to image processing. *Phys. Rev. Appl.* **2020**, *14* (3), 034001.
(62) Csaba, G.; Porod, W. Coupled oscillators for computing: A review and perspective. *Appl. Phys. Rev.* **2020**, *7* (1), 011302.
(63) Izhikevich, E. M.; FitzHugh, R. Fitzhugh-nagumo model. *Scholarpedia* **2006**, *1* (9), 1349.
(64) Cveticanin, L. On the Van der Pol oscillator: An overview. *Appl. Mech. Mater.* **2013**, *430*, 3−13.
(65) Kanamaru, T. Van der Pol oscillator. *Scholarpedia* **2007**, *2* (1), 2202.
(66) Keener, J. P. Analog circuitry for the van der Pol and FitzHugh-Nagumo equations. *IEEE Trans. Syst. Man Cybern.* **1983**, *5*, 1010−1014.
(67) Broad-band monolithic microwave active inductor and its application to miniaturized wide-band amplifiers. *IEEE Transactions on Microwave Theory and Techniques*; IEEE, 1988. Vol. *36*(12). pp 19201924.
(68) Anuar, N. *Supply clock generation (driver) circuit for 2PASCL: hara active inductor equivalent circuit and simulation*, https://nazrulanuar.com/author/wp-content/uploads/2009/04/zemi_main141.pdf.
(69) Yuan, F. CMOS active inductors and transformers. In *Principle, implementation, and applications*; Springer, 2008.
(70) Yan, Y.; Zhao, J.; Liu, Q.; Zhao, W.; Seabaugh, A.. Vertical tunnel diodes on high resistivity silicon. In *Conference Digest [Includes' Late News Papers' volume] Device Research Conference, 2004. 62nd DRC*; IEEE, 2004; pp 2728.
(71) Sicard, E.; Aziz, S. M.. *Introducing 65 nm technology in Microwind3*; HAL open science, 2011.
(72) Al-Shedivat, M.; Naous, R.; Cauwenberghs, G.; Salama, K. N. Memristors empower spiking neurons with stochasticity. *IEEE J. Emerging Sel. Top. Circuits Sys.* **2015**, *5* (2), 242−253.
(73) Seo, J.-S.; Brezzo, B.; Liu, Y.; Parker, B. D.; Esser, S. K.; Montoye, R. K.; Rajendran, B.; Tierno, J. A.; Chang, L.; Modha, D. S.. A 45nm CMOS neuromorphic chip with a scalable architecture for learning in networks of spiking neurons. In *2011 IEEE Custom Integrated Circuits Conference (CICC)*; IEEE, 2011; pp 14.
(74) Indiveri, G.; Chicca, E.; Douglas, R. A VLSI array of low-power spiking neurons and bistable synapses with spike-timing dependent plasticity. *IEEE Trans. Neural Networks* **2006**, *17* (1), 211−221.
(75) Sourikopoulos, I.; Hedayat, S.; Loyez, C.; Danneville, F.; Hoel, V.; Mercier, E.; Cappy, A. A 4-fJ/Spike Artificial Neuron in 65 nm CMOS Technology. *Front. Neurosci.* **2017**, *11*, 247370.
(76) Indiveri, G.. A low-power adaptive integrate-and-fire neuron circuit. In *Proceedings of the 2003 International Symposium on Circuits and Systems*; IEEE; 2003, Vol. *4*, pp IVIV.
(77) Mahowald, M.; Douglas, R. A silicon neuron. *Nature* **1991**, *354* (6354), 515−518.
(78) Wijekoon, J. H.; Dudek, P. Compact silicon neuron circuit with spiking and bursting behaviour. *Neural Networks* **2008**, *21* (2−3), 524−534.
(79) Yamazaki, K.; Vo-Ho, V.-K.; Bulsara, D.; Le, N. Spiking neural networks and their applications: A Review. *Brain Sci.* **2022**, *12* (7), 863.
(80) Tavanaei, A.; Ghodrati, M.; Kheradpisheh, S. R.; Masquelier, T.; Maida, A. Deep learning in spiking neural networks. *Neural Networks* **2019**, *111*, 47−63.
(81) Zenke, F.; Ganguli, S. Superspike: Supervised learning in multilayer spiking neural networks. *Neural Comput.* **2018**, *30* (6), 1514−1541.
(82) Wijesinghe, P.; Srinivasan, G.; Panda, P.; Roy, K. Analysis of liquid ensembles for enhancing the performance and accuracy of liquid state machines. *Front. Neurosci.* **2019**, *13*, 504.
(83) Yamazaki, T.; Tanaka, S. The cerebellum as a liquid state machine. *Neural Networks* **2007**, *20* (3), 290−297.
(84) Roy, S.; Basu, A.; Hussain, S.. *Hardware efficient, neuromorphic dendritically enhanced readout for liquid state machines*; IEEE, 2013; pp 302305.
(85) Schrauwen, B.; D'Haene, M.; Verstraeten, D.; Van Campenhout, J.. *Compact hardware for real-time speech recognition using a liquid state machine*; IEEE, 2007; pp 10971102.
(86) Maass, W.; Natschläger, T.; Markram, H. Real-time computing without stable states: A new framework for neural computation based on perturbations. *Neural Comput.* **2002**, *14* (11), 2531−2560.
(87) Maass, W.. On the Computational Power of Recurrent Circuits of Spiking Neuron; Technische Universität Graz, 2000.
(88) Agarwal, K.; Nassif, S.. Characterizing process variation in nanometer CMOS. In *Proceedings of the 44th annual Design Automation Conference*; IEEE, 2007; pp 396399.

https://doi.org/10.1021/acsomega.3c09936
ACS Omega 2024, 9, 18062−18071